

Figure 5.88 Liner Specimen at Tear #15

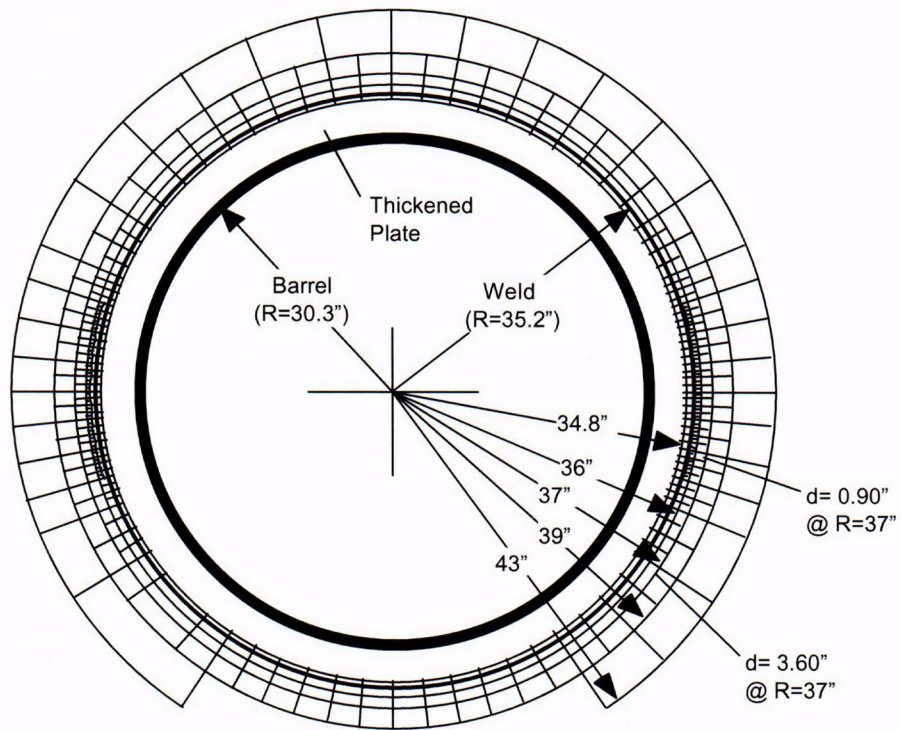
8. Tensile and hardness tests on welded test samples indicated that modest amounts of plastic strain localization should be expected in the weld-heat-affected zones, but to a much lesser extent than observed in association with the liner tears. Consistent with this, smaller (but significant) amounts of localized plastic strain were observed adjacent to some welds that had not been repaired or ground. These strains were sufficient to initiate necking in the most severely strained regions. However, with the possible exception of tear #12, there was no indication that tearing was imminent in regions other than those where repair welding and substantial grinding had been done.
9. The mechanical testing results did not suggest that deficiencies in the properties of either the base metal or weld metal, nor excessive softening in the weld-heat-affected zones, could account for the extensive localized plastic deformation culminating in tearing that appeared to occur in the liner.

In summary, it is apparent that the onset of liner tearing at $2.5P_d$ resulted, to a significant degree, from the difficulty of field welding the very thin liner. The conditions that led to the liner tearing would not be present to the same degree in the prototype, and the initiation of tearing might be delayed until a higher pressure was achieved. Nevertheless, in spite of the liner welding difficulties, it is also apparent that the near field strains in the vicinity of a liner discontinuity must be large enough to initiate a tear because all the tears were initiated at vertical weld seams within the middle portion of the cylinder wall.

5.3.2.2.3 Posttest Measurements

As described in Section 3.2.5.4, a grid was constructed around the E/H to measure the residual strain field after the test. The pretest analysis predicted large strains near the perimeter of the thickened insert plate surrounding the E/H barrel and near the anchors and stiffeners that terminated near the insert. The grid, shown in Figure 5.89, was drawn, and the position of the grid points was obtained using a 3D digital position mapping tool. After the LST, the grid points were mapped again and the pre- and posttest positions were plotted in Figure 5.90.

Unfortunately, as noted previously, the strains in this region were very small and the resulting residual displacements are barely distinguishable from the pretest positions, given the precision of the digital probe. As a result, no useful information was obtained by this effort.



E/H Inside View

Figure 5.89 E/H Displacement Grid

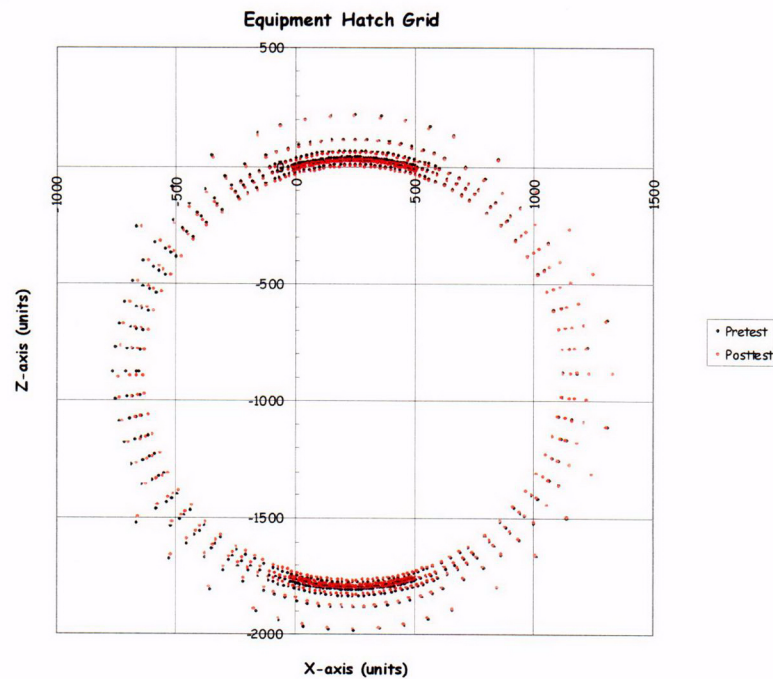


Figure 5.90 E/H Post-LST Displacement

5.3.3 Structural Failure Mode Test Results

5.3.3.1 Test Data

The Structural Failure Mode Test data (DYN only) is provided on the enclosed data CD in Excel® spreadsheets, as noted in Section 5.3.1. The response of every functioning transducer in the revised instrumentation suite is provided. The following sections present a synthesis of the data focusing on the critical response measurements.

5.3.3.1.1 Displacements

As for the LST, the displacement data provides the most comprehensive view of the overall or global response of the model. Since the displacement transducers had to be waterproof, a reduced suite of gages was used during the SFMT. Based on the results of the LST, two vertical arrays at Azimuth 135 degrees and 324 degrees, and one horizontal array at Elev. 4680, were employed for the SFMT, as shown in Figure 5.26. Figures 5.91 through 5.93 show the radial displacement response as a function of pressure along these cardinal lines. Since the displacement transducers had to be removed after the LST to install the elastomeric liner and new transducers were installed for the SFMT, the displacements were 'zeroed' prior to the start of the SFMT on November 6, before filling the vessel with water. The displacements therefore reflect only the response to pressure (including the hydrostatic pressure) and not the effects of prestressing, nor any other previous loading. Note that the pressures shown are the effective pressure, i.e. the volume weighted average pressure in the model.

During the SFMT, the displacement response of the model is essentially linear to just beyond 3.0 Pd, when global yielding begins to occur prior to rupture. The initial stiffness of the model, however, is less than the initial stiffness during the LST. Figure 5.94 compares the response at the mid-height of the cylinder (Z6) during the LST and the SFMT. (The SFMT response was offset in this figure by adding the residual displacement at the end of the LST to facilitate comparison.) This figure shows that the hoop stiffness during the SFMT is essentially identical to the post-cracking stiffness during and after the LST. It also shows that the SFMT displacement is nearly identical to the LST displacement at the maximum LST pressure, suggesting that, if the LST had continued, the response would have been virtually

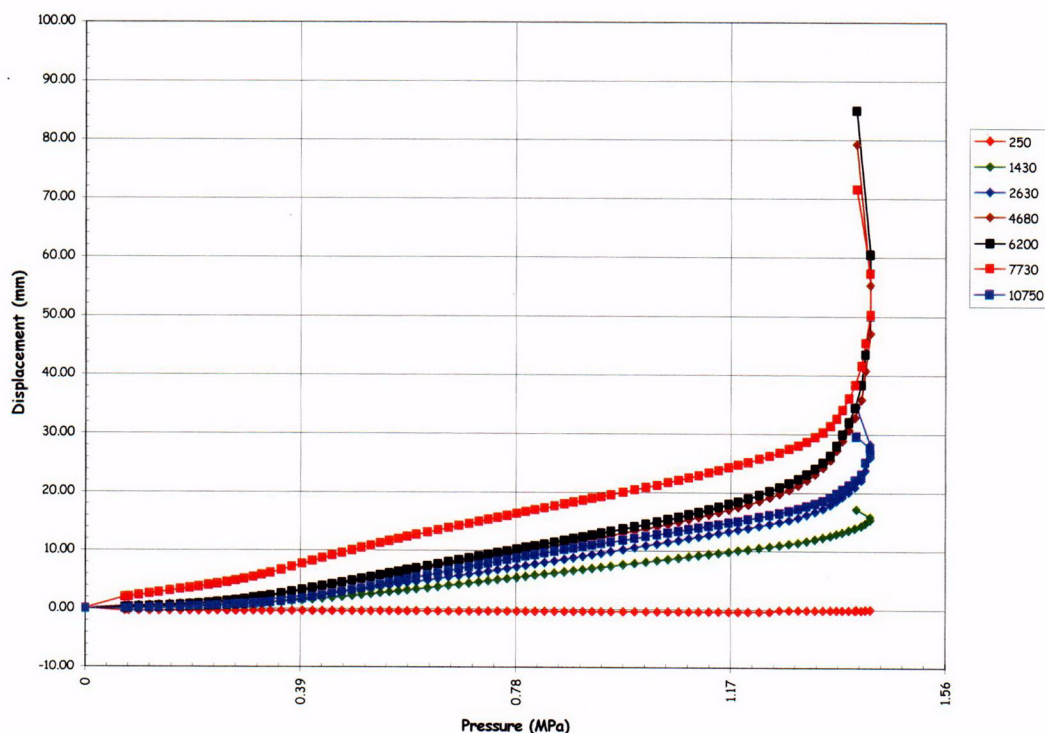


Figure 5.91 SFMT – Radial Displacement at Azimuth 135 degrees (Z)

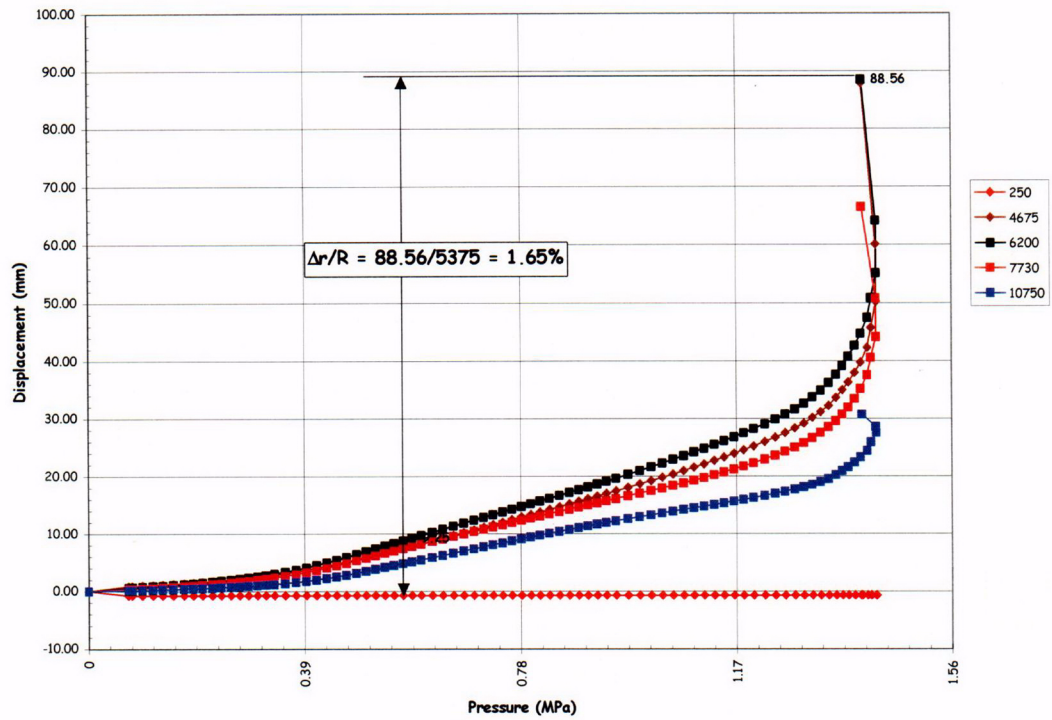


Figure 5.92 SFMT – Radial Displacement at Azimuth 324 degrees (L)

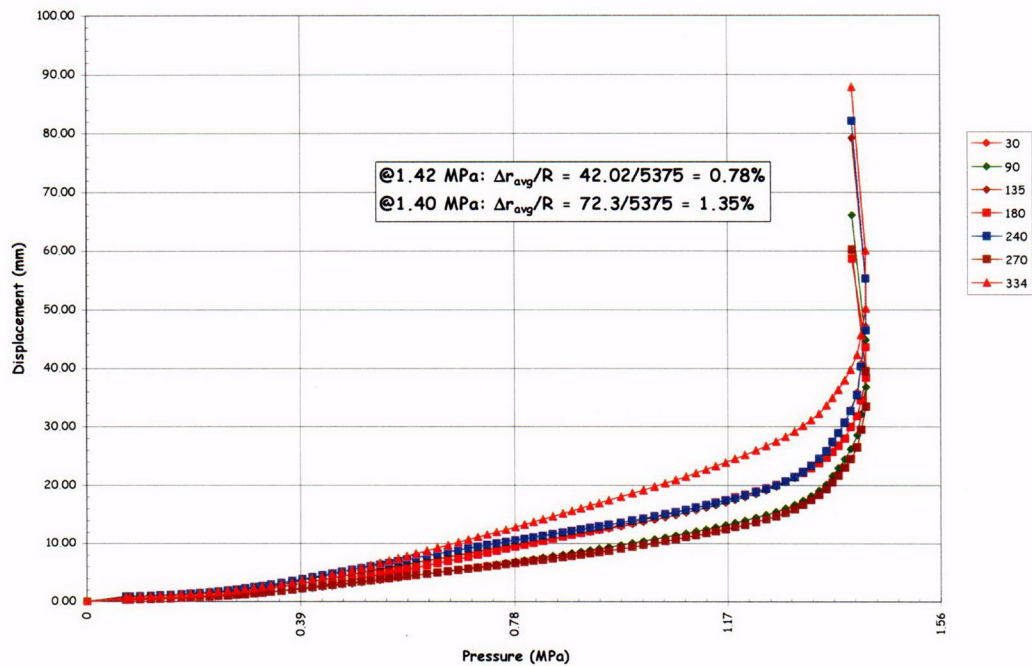


Figure 5.93 SFMT – Radial Displacement at Elev. 4680 (5)

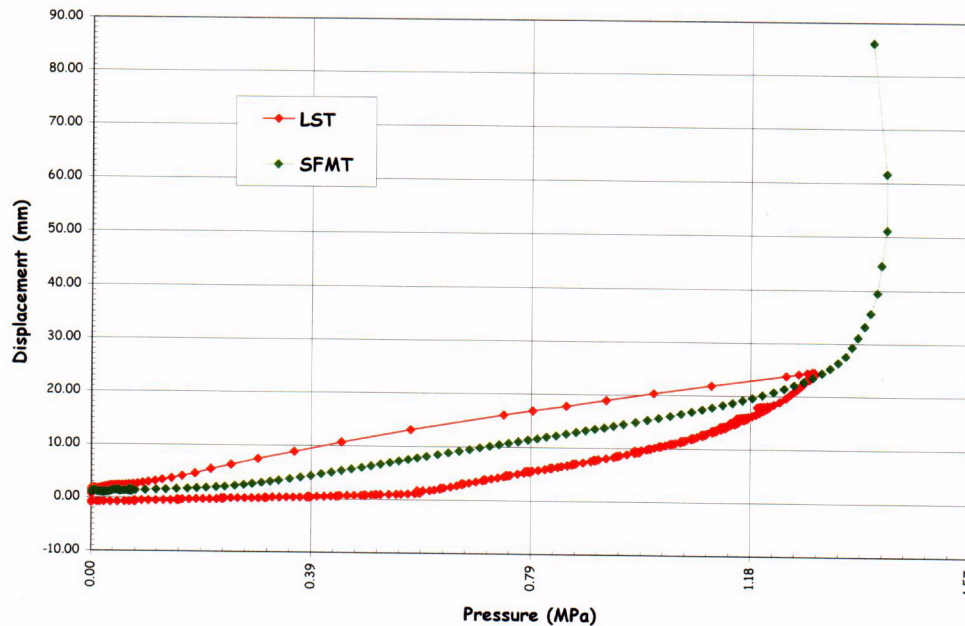


Figure 5.94 SFMT – Radial Displacement at Azimuth 135 degrees, Elev. 6200

identical to that measured during the SFMT. Similarly, the vertical displacements at the apex (offset again) are compared in Figure 5.95.

Since the SFMT was conducted as a continuous pressure test with no holds for gage stability of leak checks, there were no discontinuities in the response histories.

The peak displacements shown in the plots were the final readings obtained before the model ruptured and the gages were destroyed. The pressure values at and beyond the peak were recorded at the beginning of the data scan. Since each scan took approximately 30 seconds, the pressure may have increased (or decreased) during the scan. Note that a few data scans were completed after the peak pressure was reached. The post-peak values may indicate some ‘softening’ of the model. However, it is more likely that the plots reflect the drop in pressure due to the rapid expansion and increasing leakage just prior to rupture.

Figure 5.92 displays the displacements at Azimuth 324 degrees, which coincides with the centerline of the E/H. The largest radial displacement recorded during the SFMT, 88.56 mm, again occurred at this azimuth at elev. 6200, above the E/H. Computing the equivalent hoop strain due to pressure at this location from kinematics,

$$@P_{\text{final}} = 3.58P_d: \frac{\Delta r}{R} = \frac{88.56}{5376} = 1.65\%$$

At the peak pressure, $3.65P_d$, the displacement was 55.12 mm, yielding an equivalent hoop strain of 1.02%

Figure 5.93 compares the displacement response as a function of azimuth at elev. 4680, nominally the mid-height of the cylinder and the centerline of the E/H, A/L, and M/S penetrations. The response is not as uniform as was observed during the LST. Nonetheless, averaging the radial deformation due to pressure yields a nominal average hoop strain of 0.78% at the peak pressure $3.65P_d$. Similarly, the average hoop strain at $3.58P_d$, just prior to rupture, was 1.35%.

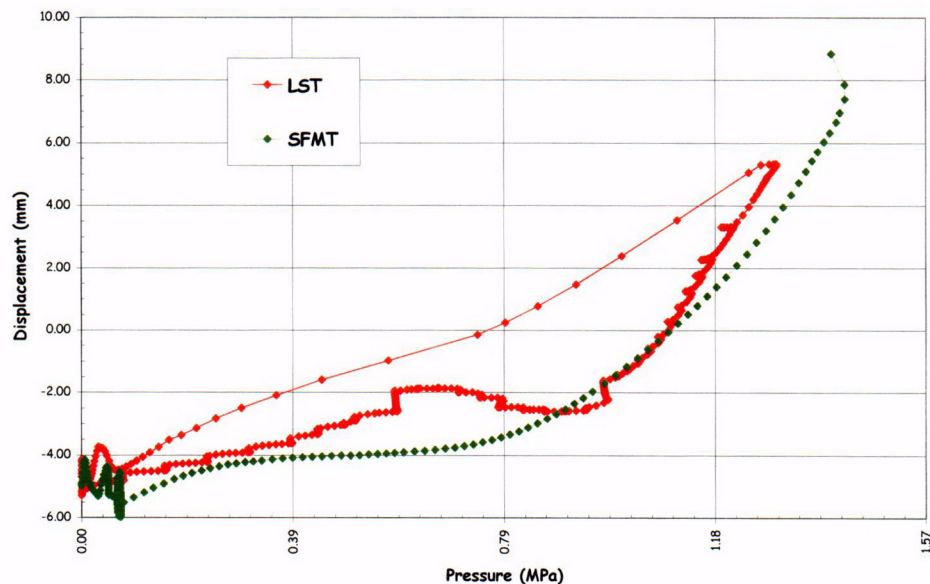


Figure 5.95 SFMT – Vertical Displacement at Apex

The vertical displacements are shown in Figure 5.96. The maximum vertical displacement at the springline was 10.84 mm at Azimuth 135 degrees, essentially the same as during the LST, and 5.94 mm at Azimuth 324 degrees, less than during the LST. The reason for the small displacement at 324 degrees is not immediately obvious; however, it might be the stiffening effect of the E/H embossment, although this was not observed during the LST. Nevertheless, it is clear that the vessel did not yield in the vertical direction and the vertical strains were still on the order of 0.1%.

Deformed profiles of the PCCV model, constructed from the displacement data in a similar manner as those constructed for the LST, are shown in Figures 5.97 through 5.100. For the SFMT, the initial position was again assumed to be defined by the as-built model survey data (Appendix C). However, since the gages were zeroed prior to the start of the SFMT, any deformations of the liner surface or the wall are not reflected in the data.

The as-built position of the PCCV model is plotted in the first portion of the figures, along with the deformed shapes due to the hydrostatic pressure (H_2O) and at approximately $1.0P_d$, $2.0P_d$, $2.5P_d$, $3.0P_d$, $3.5P_d$, and $P_{max} = 3.63P_d$. The second portion of each figure provides a more refined breakdown between $3.0P_d$ and $3.63P_d$ and the profile at $P_{final} = 3.57P_d$, immediately prior to rupture of the vessel. These figures dramatically illustrate the large deformations that occur as the vessel yields, even though the pressure is dropping. The displacement nearly doubles as the pressure drops from $3.63P_d$ to $3.57P_d$.

A most provocative observation after considering the displacement data and the global response of the model is that the relatively small pressure increase between the LST and the SFMT, from $3.3P_d$ to $3.6P_d$ (approximately 10%), made the vessel go from a relatively benign and only slightly damaged step to total collapse. It is reasonable to speculate what the response of the model might have been if the liner had not torn and leaked at $2.5P_d$, arguably prematurely, and it had been possible to pressurize it to $3.6P_d$ pneumatically.

5.3.3.1.2 Liner Strains

Since the liner was damaged during the LST and large portions were removed for metallographic analysis, the response of the liner was not a critical objective during the SFMT. Nevertheless, 18 exterior gages (the interior ones were

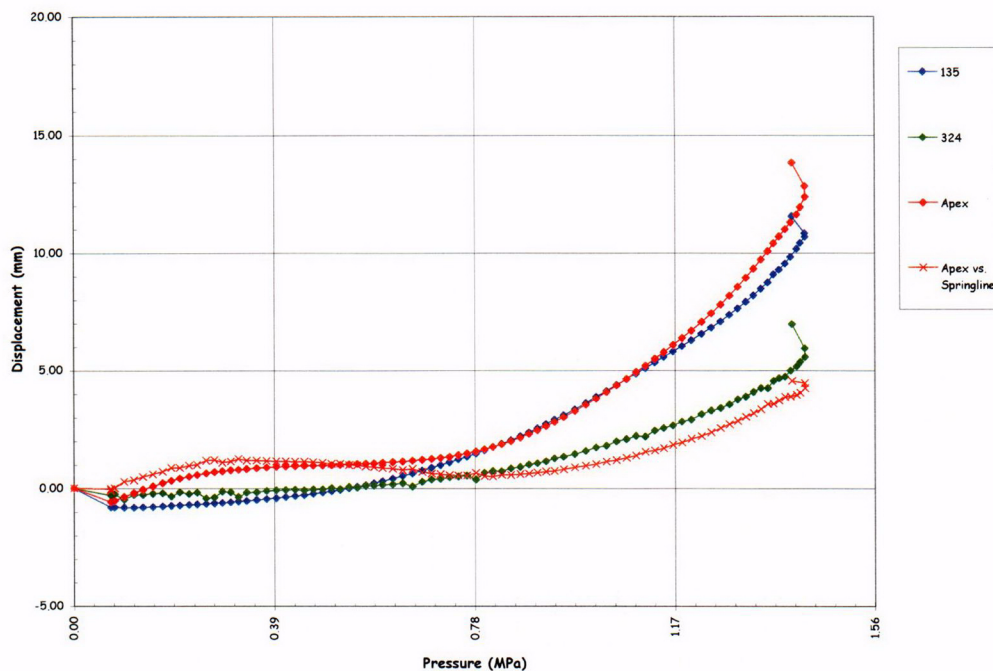


Figure 5.96 SFMT Vertical Displacements at Springline (El. 10750) and Apex

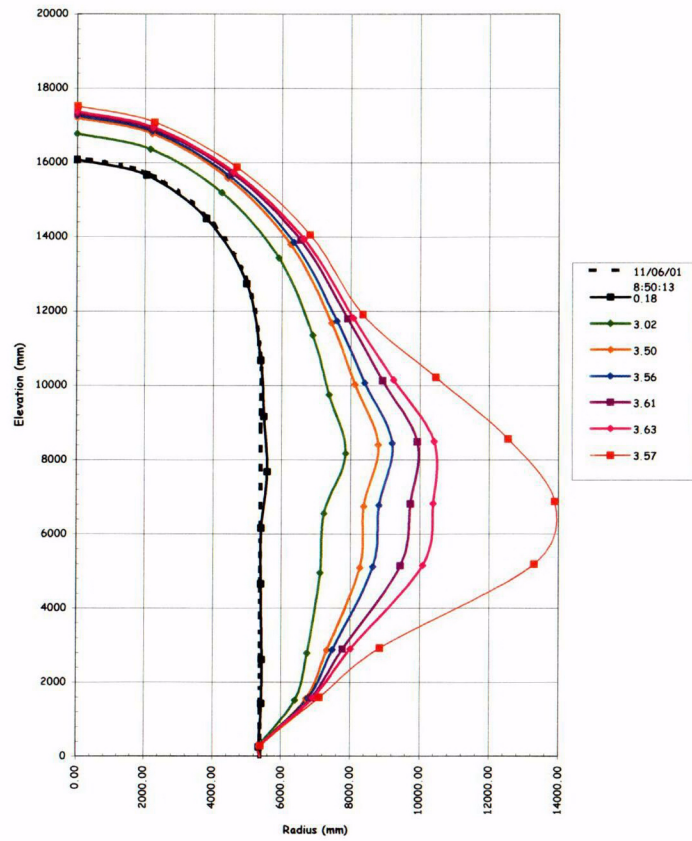
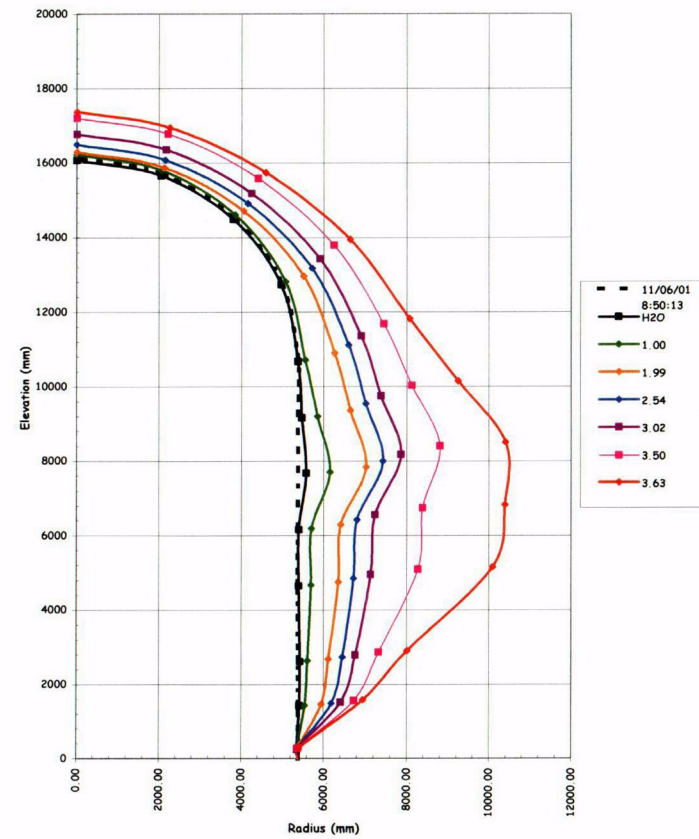
removed prior to installing the elastomeric liner) were monitored during the SFMT to provide some information on the liner response at higher pressures and for comparison with other instruments. Of the 18 strain gages selected, three failed

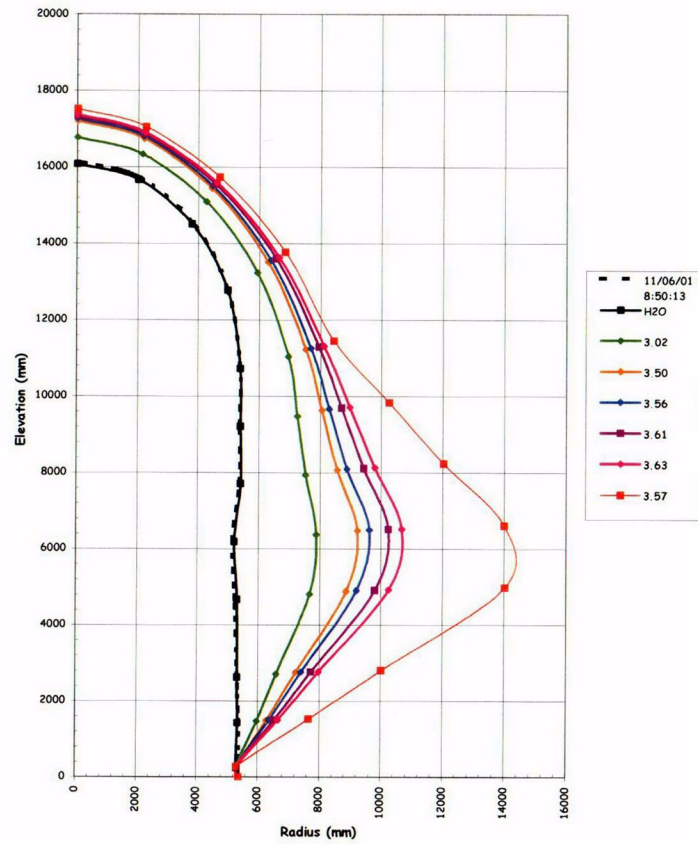
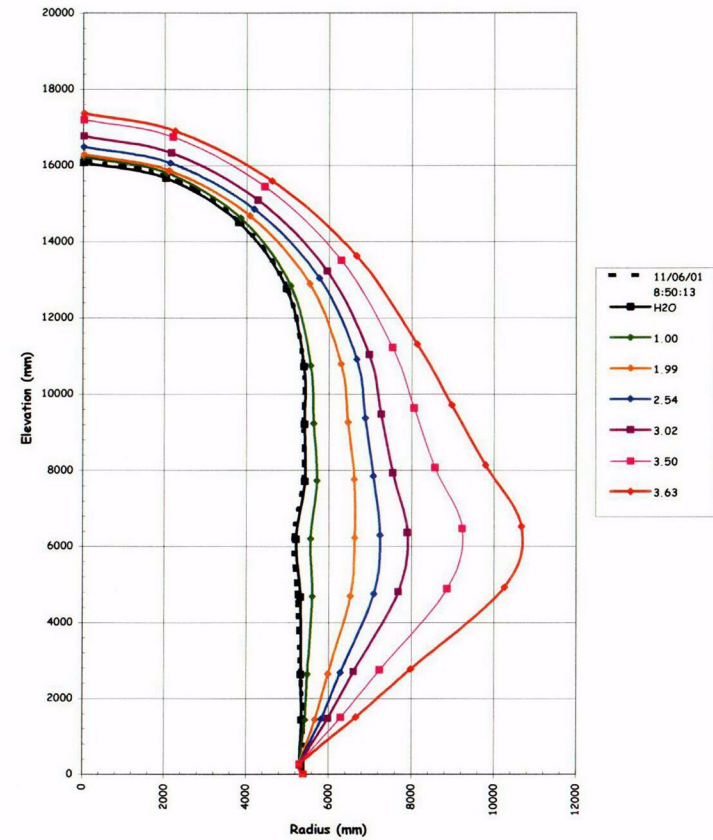
before filling the model with water. The remaining gages at the wall-base junction and the two external gages at D7 also appeared to have been damaged prior to the test, possibly by water leaking from the model. As a result, meaningful data was only obtained for three liner strain gages.

The strain histories for the surviving gages are plotted in Figure 5.101. These gages measured the hoop liner strain inside a rathole (see drawing D-SN-P-209, Appendix E) at Azimuth 0 degrees, elev. 7730 (A7) and Azimuth 135 degrees, elev. 4680 and 6200 (Z5 and Z6) at the mid-height of the cylinder. The maximum liner strains at Z5 (1.9%) and Z6 (1.5%) are consistent with the strains calculated from the displacements. At A7, nearest the location where the model ruptured, the hoop strains were consistently lower than those at Z5 and Z6, even going into compression, until the peak pressure was reached, when the strain increased rapidly to a maximum of 1.5% tension. While these were not free-field gages, they nevertheless gave some indication of the hoop strains in the liner.

5.3.3.1.3 Rebar and Concrete Strains

Eighty-two rebar and gage bar gages were selected for monitoring during the SFMT. Of these, four of the main rebar strain gages and all the gage bar strain gages appear to have failed before $0.5P_d$. The strain histories for all 31 surviving rebar gages are shown in Figures 5.102 to 5.104. The maximum free-field hoop rebar strain was 1.4% (RS-C-Z6-02). The maximum free-field meridional rebar strain was 0.3% (RS-M-D6-02). These values are consistent with the global strains based on displacement data. The rebar strains at the wall-base junction show the effect of bending but combined with the other meridional strains, confirm that the model was still essentially elastic in the vertical direction.

(a) $0P_d$ to $3.63P_d$ (b) $3.0P_d$ to $3.63P_d$ Figure 5.97 SFMT - Deformation at Azimuth 135 Degrees (Z) $\times 100$

(a) $0P_d$ to $3.63P_d$ (b) $3.0P_d$ to $3.63P_d$ Figure 5.98 SFMT - Deformation at Azimuth 324 Degrees (L) \times 100

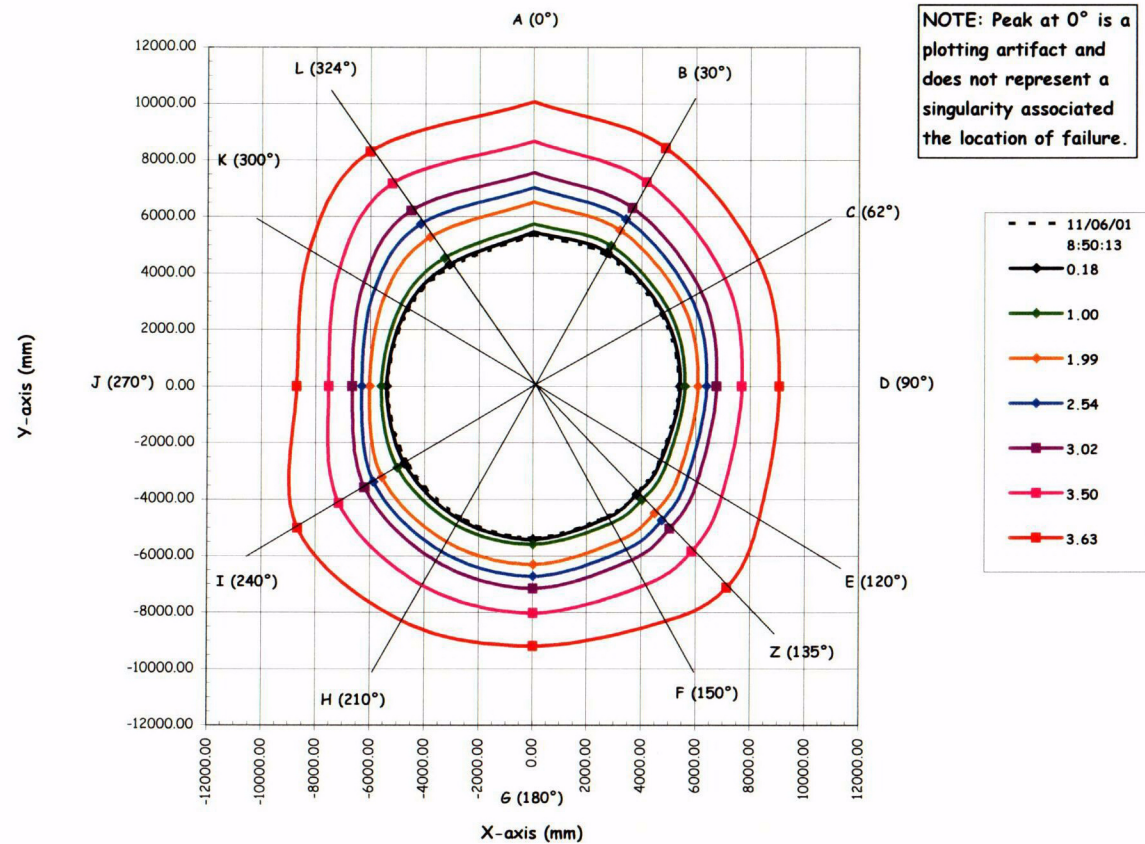


Figure 5.99 SFMT - Deformation at Elev. 4680 (5) \times 100 - $0P_d$ to $3.63P_d$

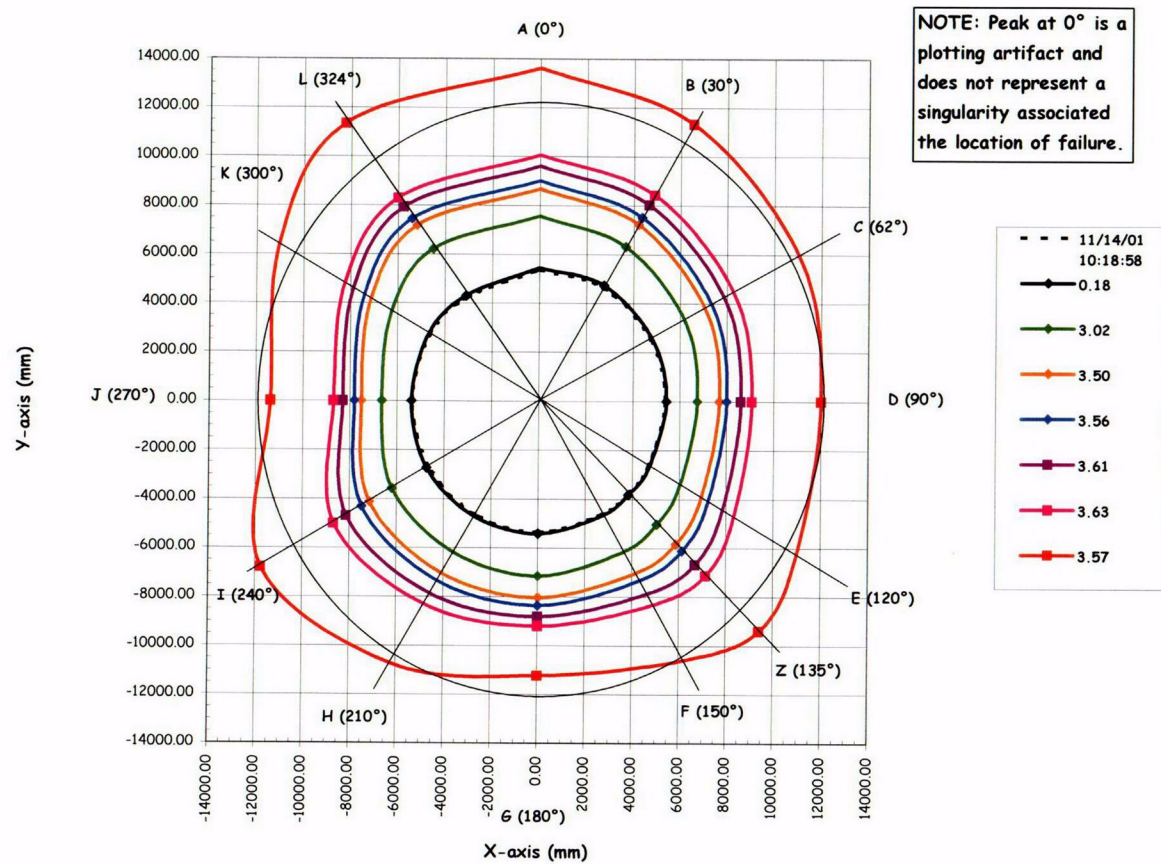


Figure 5.100 SFMT - Deformation at Elev. 4680 (5) \times 100 - 3.0P_d to 3.63P_d

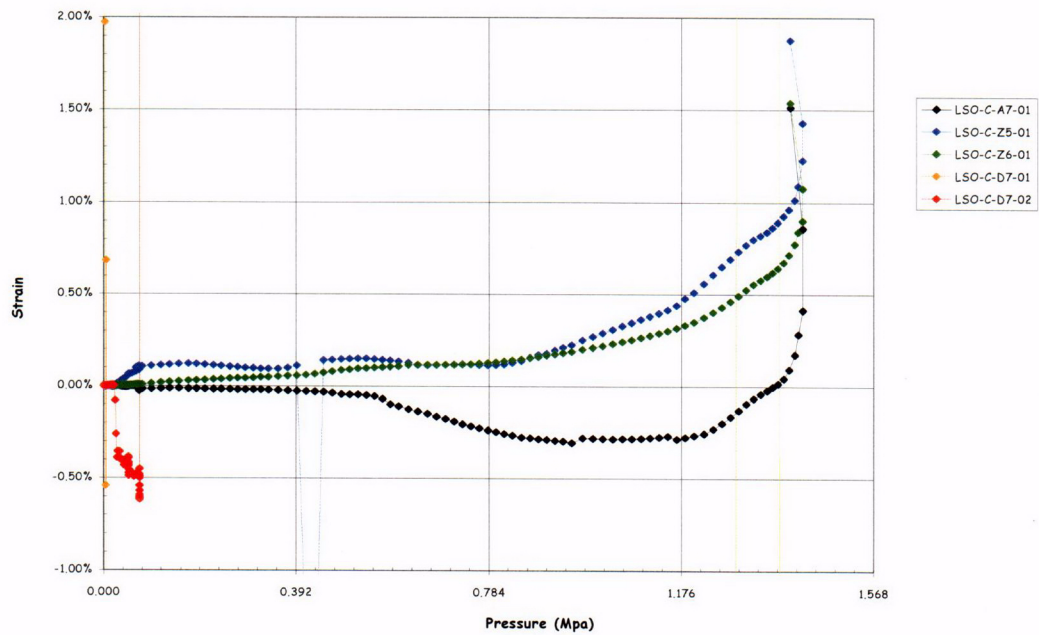


Figure 5.101 SFMT Exterior Liner Strains

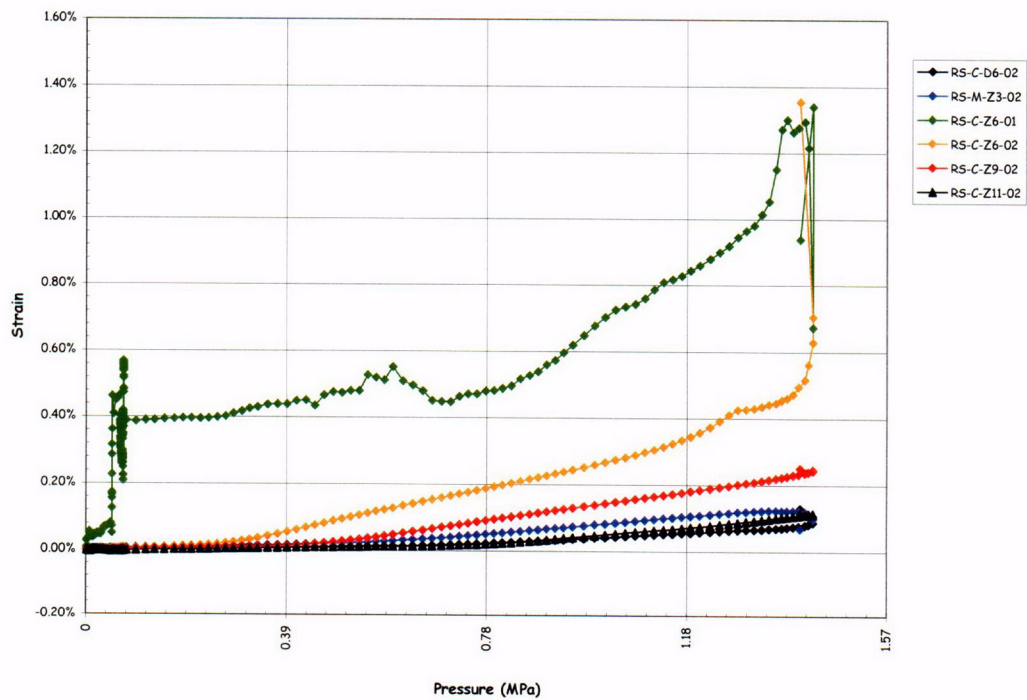


Figure 5.102 SFMT – Free-Field Hoop Rebar Strains

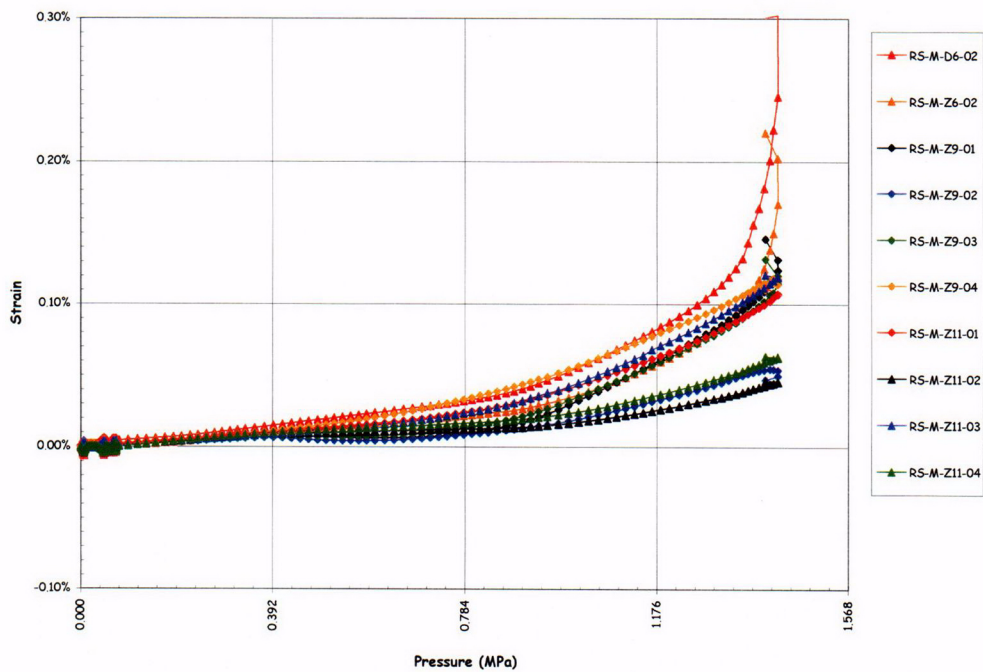


Figure 5.103 SFMT – Free-Field Meridional Rebar Strains

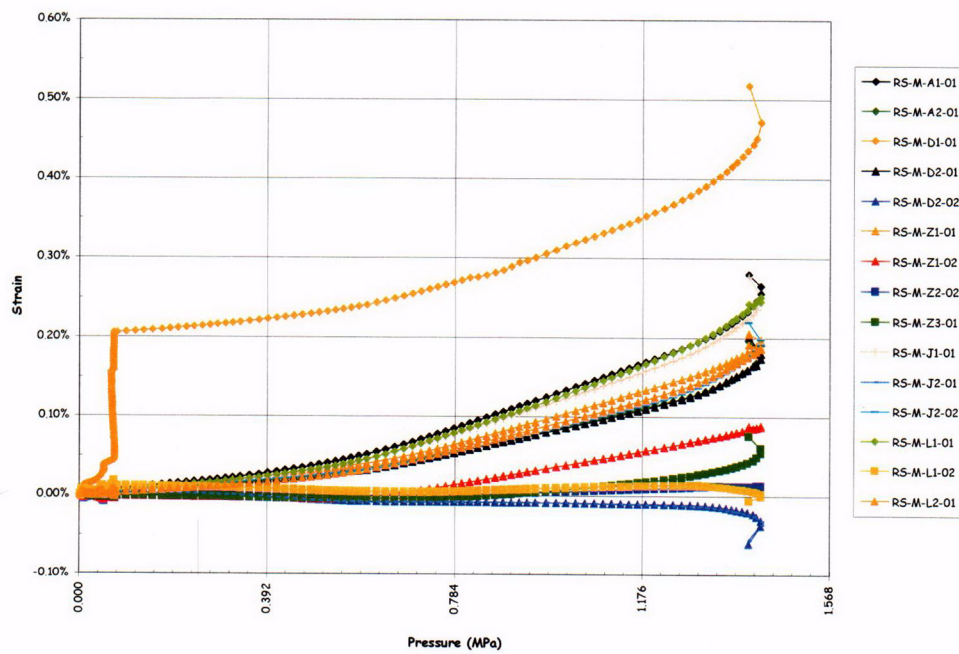


Figure 5.104 SFMT – Meridional Rebar Strains at Wall-Base Junction

Concrete strains, measured by the surviving SOFO fiber-optic gages, are plotted in Figure 5.105. The maximum hoop strain in the concrete, 1.1% (CE-C-Z6-01) at the mid-height of the cylinder, is a little lower than the displacement-based or rebar strains, but overall the concrete strains are consistent with the other measurements.

5.3.3.1.4 Tendon Forces and Strains

All the tendon load cells and strain gages that survived the LST were still functioning at the start of the SFMT and all were monitored during the test. Several load cells and tendon strain gages failed after filling the PCCV with water or early during the SFMT, presumably due to water leaks from the model damaging the gage or shorting out the wiring. The data for all the gages that were functioning at the start of the test are provided, however.

Figures 5.106 and 5.107 show the anchor forces for the instrumented tendons during the SFMT. These anchor forces are representative examples of all the tendon anchors. With the exception of one anchor on H53, the hoop tendon anchor forces increase to nearly 600 kN, which is close to the breaking strength of straight tendons in laboratory tests. It is reasonable to expect that the breaking strength of the curved tendons under field conditions would be lower than the laboratory breaking strength. Load cell TL-C-J6-01 on H53 exhibits an artificially high force near the beginning of the SFMT, most likely from moisture affecting the gage. However, the increased force due to pressure tracks very closely with the other load cells. The vertical tendon anchor forces do not show as large an increase, and the average maximum force only approaches 500 kN, well below the breaking strength. This is consistent with response during the LST and the observation that the vertical tendons did not fail prior to the rupture of the model.

Near the end of the test, sudden decreases in load were observed for several hoop tendon load cells and interpreted as individual strand wires breaking. After reaching the peak pressure, all the load cell readings dropped sharply as the tendons and the model ruptured.

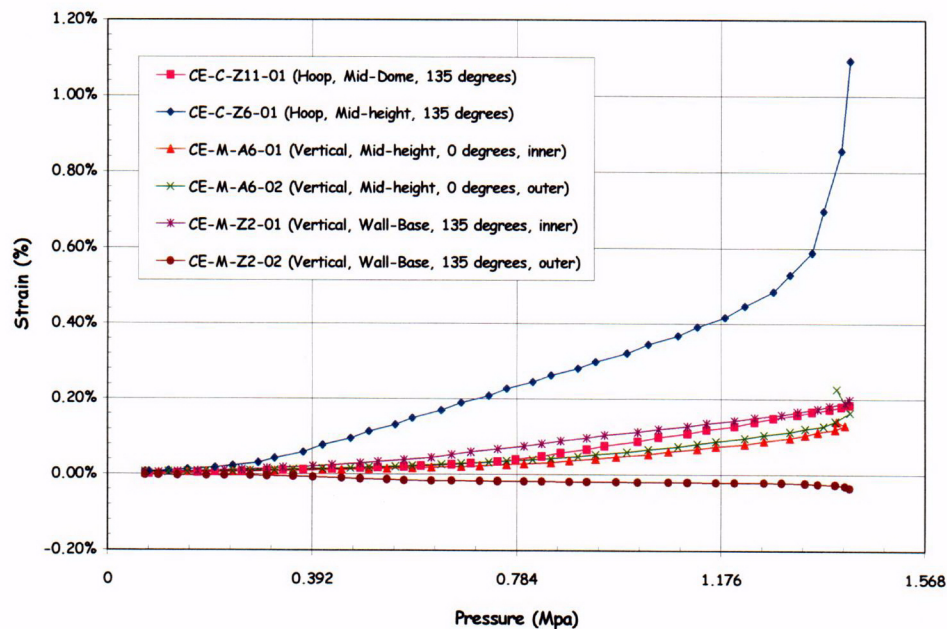


Figure 5.105 SFMT – Concrete (SOFO) Strains

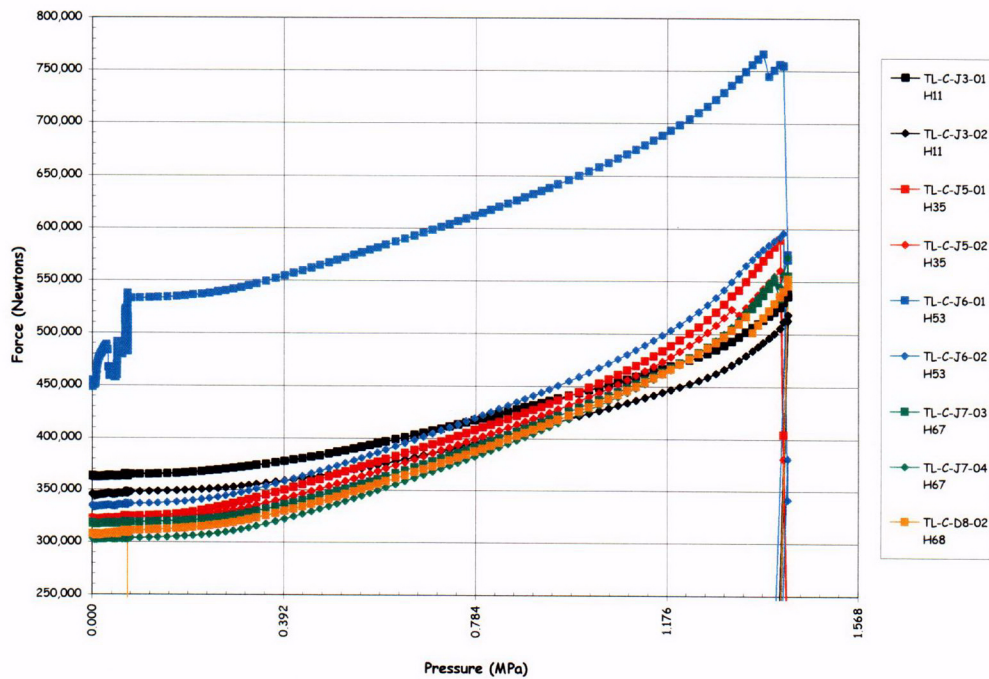


Figure 5.106 SFMT – Instrumented Hoop Tendon Anchor Forces

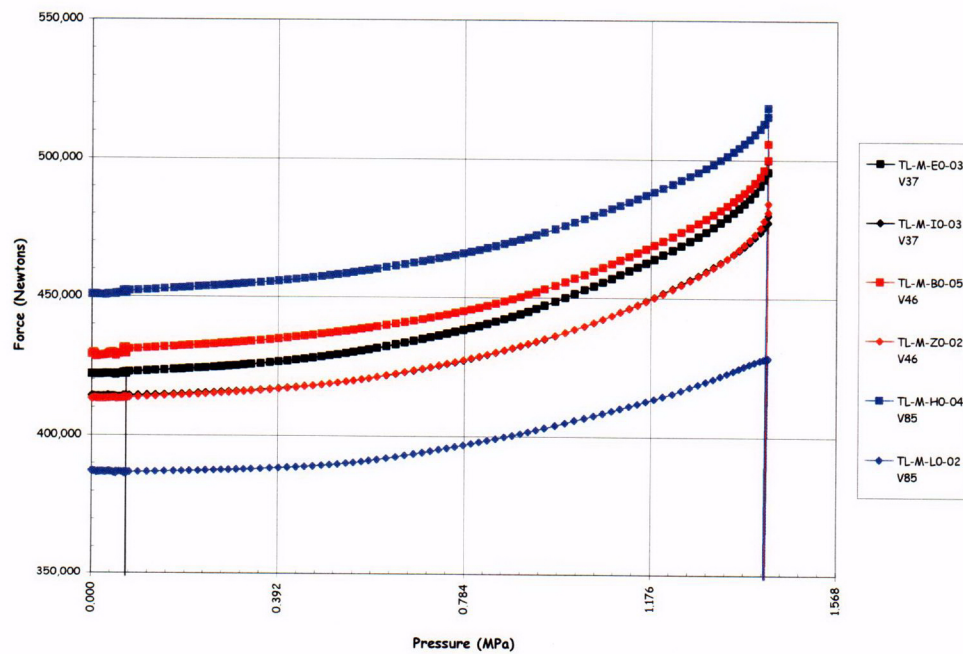


Figure 5.107 SFMT – Instrumented Vertical Tendon Anchor Forces

Tendon strains were also recorded using the surviving foil gages mounted on individual strand wires. Figures 5.108 and 5.109 show the strains for hoop tendons H53 and H68, and Figure 5.110 shows the strains for vertical tendon V46. These results are typical of the other instrumented tendons, although the magnitude of the strains vary. Since the strain gages were 're-zeroed' before the SFMT, only the strain due to pressure is plotted. The total tendon strain is the measured strain plus the residual prestressing strain, typically on the order of 0.4% for the hoop tendons and 0.6% for the vertical tendons. The hoop tendon strains at maximum pressure were therefore on the order of 1.0%, 0.4% due to prestressing plus 0.6% due to the maximum pressure of $3.65P_d$. Similarly, the maximum hoop tendon strain measure prior to rupture is on the order of 1.4% to 1.5%. There may be some local strain concentrations that were not captured by the strain gages, but this limiting tendon strain is significantly less than the ultimate strain obtained from laboratory tests of a straight tendon sample, typically on the order of 4% for the tendon and 7% for individual strands. Furthermore, none of the model tendons ruptured at the anchors where strain concentrations might be expected, but all ruptured where the deformation of the model was greatest, approximately azimuth 6 degrees.

Similarly, the strain in the vertical tendons at the maximum pressure are on the order of 0.1 to 0.2%, and the total strain is on the order of 0.7% to 0.8%. Both are well below the strain at which the hoop tendons were believed to have ruptured, reinforcing the belief that the vertical tendons did not fail prior to the rupture of the vessel.

The tendon force profiles, previously constructed for prestressing and the LST, were also constructed for the SFMT. Since the tendon strains were re-zeroed for the SFMT, it was assumed that the residual strain for each gage after the LST was the initial strain at the start of the SFMT. These residual strain values were added to the SFMT strain data and the force distribution profiles were constructed in the same manner as before. Figures 5.111 to 5.115 show the force profiles for the five instrumented hoop tendons.

One point deserves mentioning. The tendon anchor forces appear to drop off at or just beyond the peak pressure. This is an artifact of rupture occurring during a data scan. The pressure and strain values were recorded near the beginning of the scan, while the load cells were among the last instruments scanned. If rupture, which occurred in a few seconds, took place during the 30 second data scan, the DAS would associate the pressure before rupture with the load cell reading after rupture, giving the appearance that the tendon anchor forces dropped before the model ruptured.

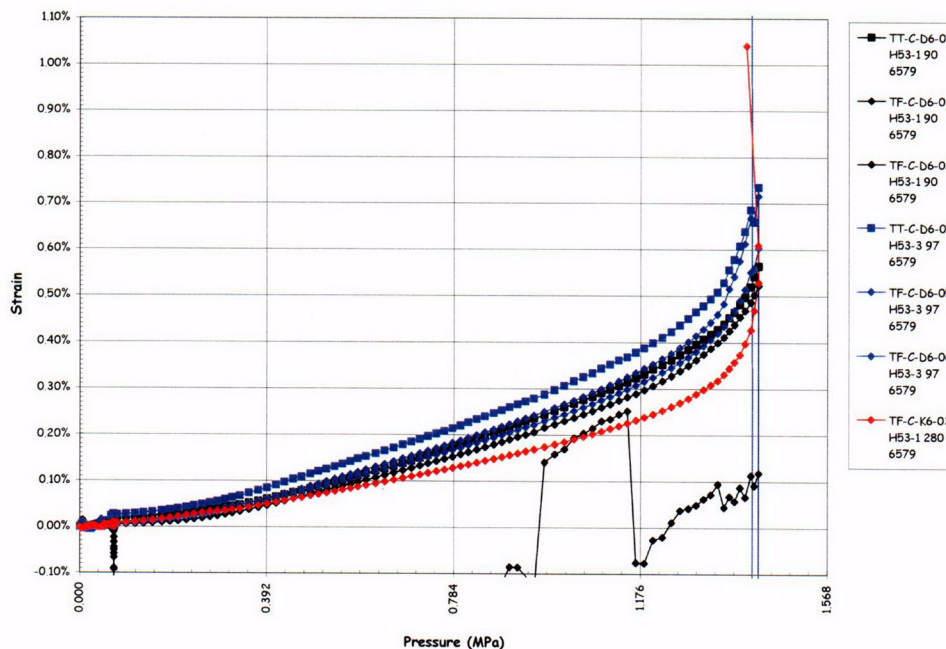


Figure 5.108 SFMT – Tendon H53 Strains

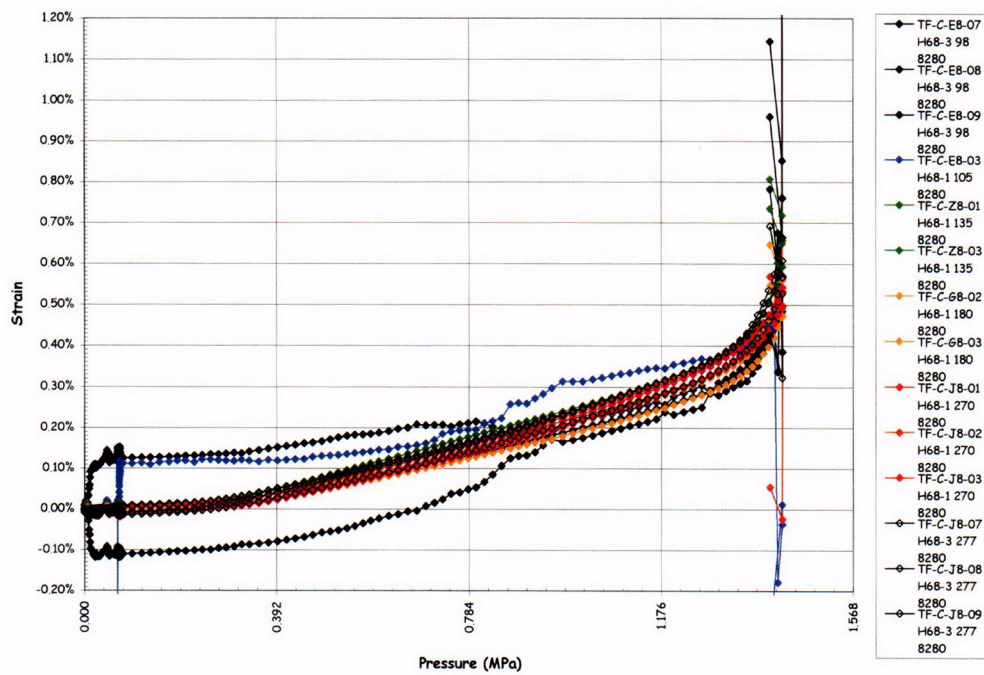


Figure 5.109 SFMT – Tendon H68 Strain

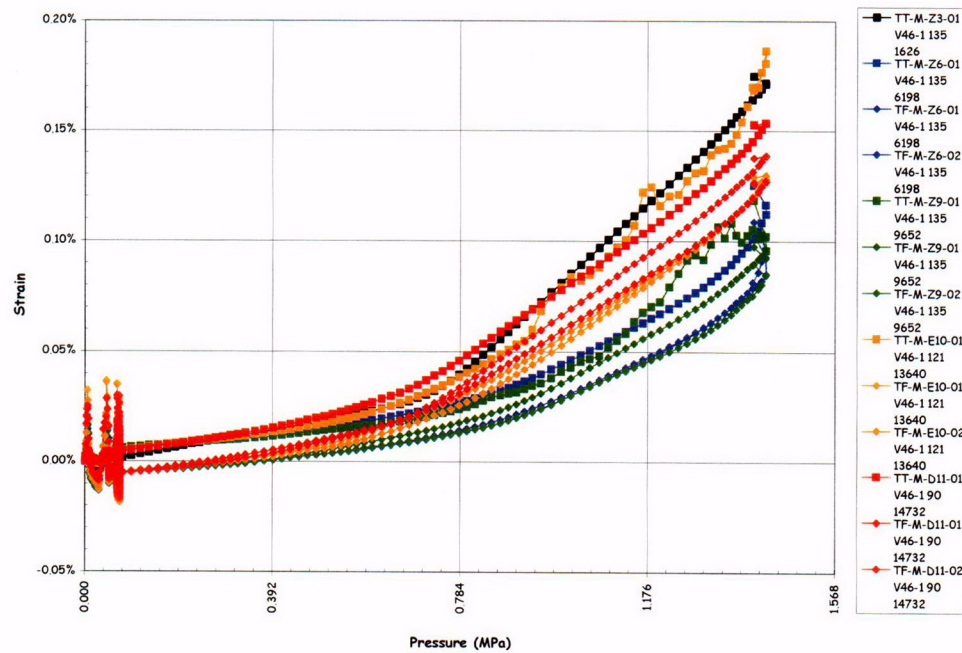


Figure 5.110 SFMT – Tendon V46 Strains

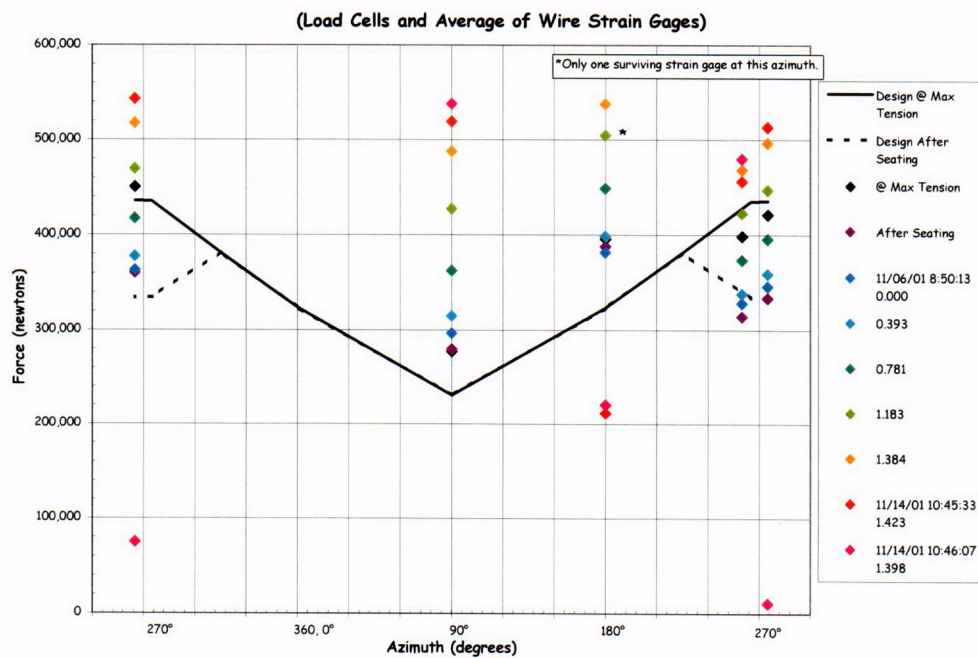


Figure 5.111 SFMT – Tendon H11 Force Distribution (Elev. 1854)

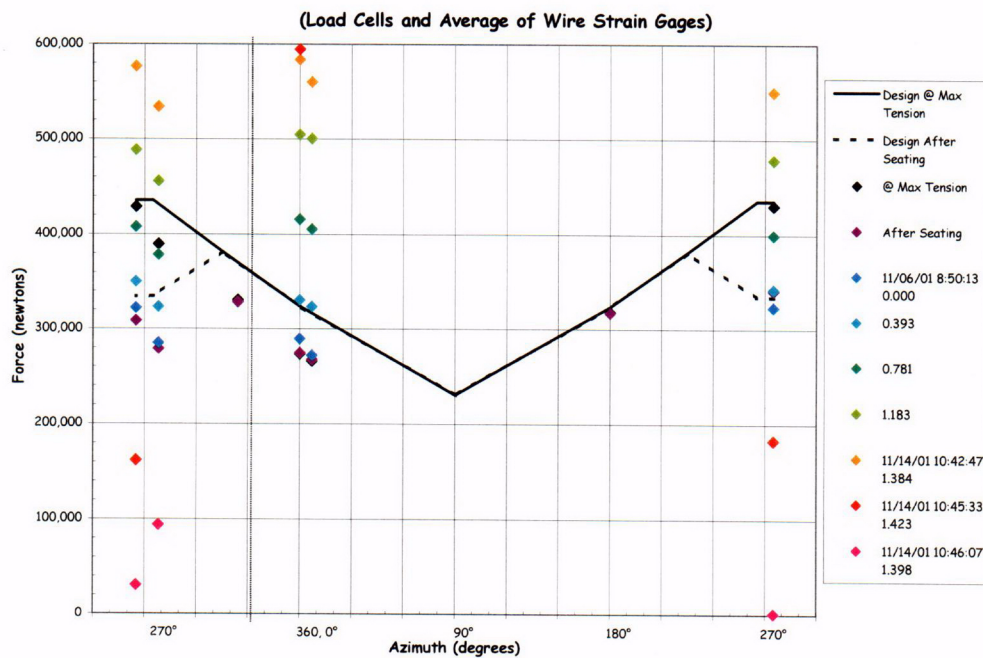


Figure 5.112 SFMT - Tendon H35 Force Distribution (Elev. 4572)

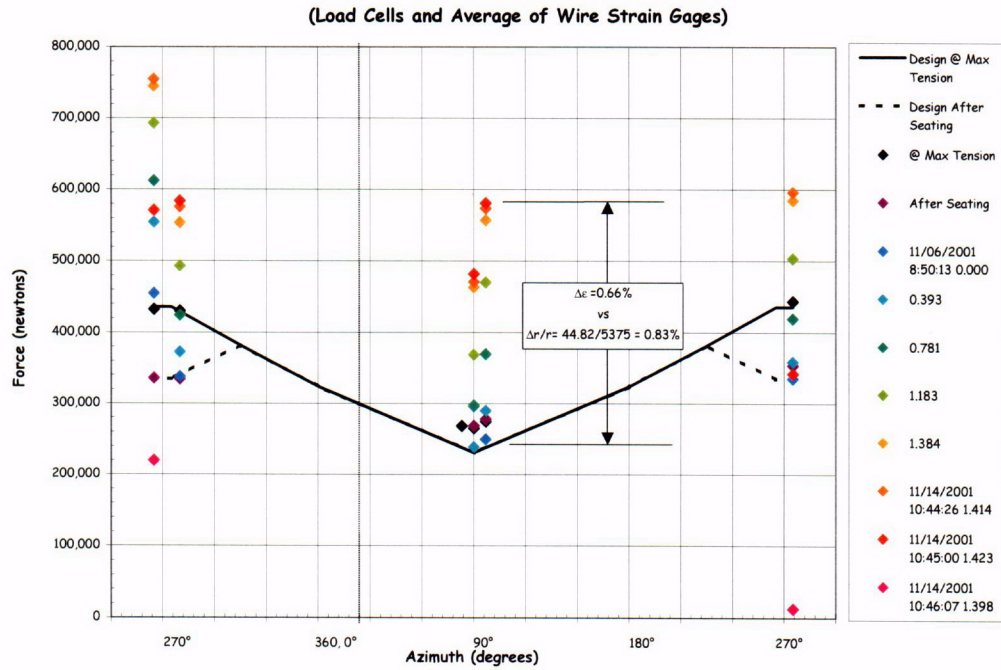


Figure 5.113 SFMT - Tendon H53 Force Distribution (Elev. 6579)

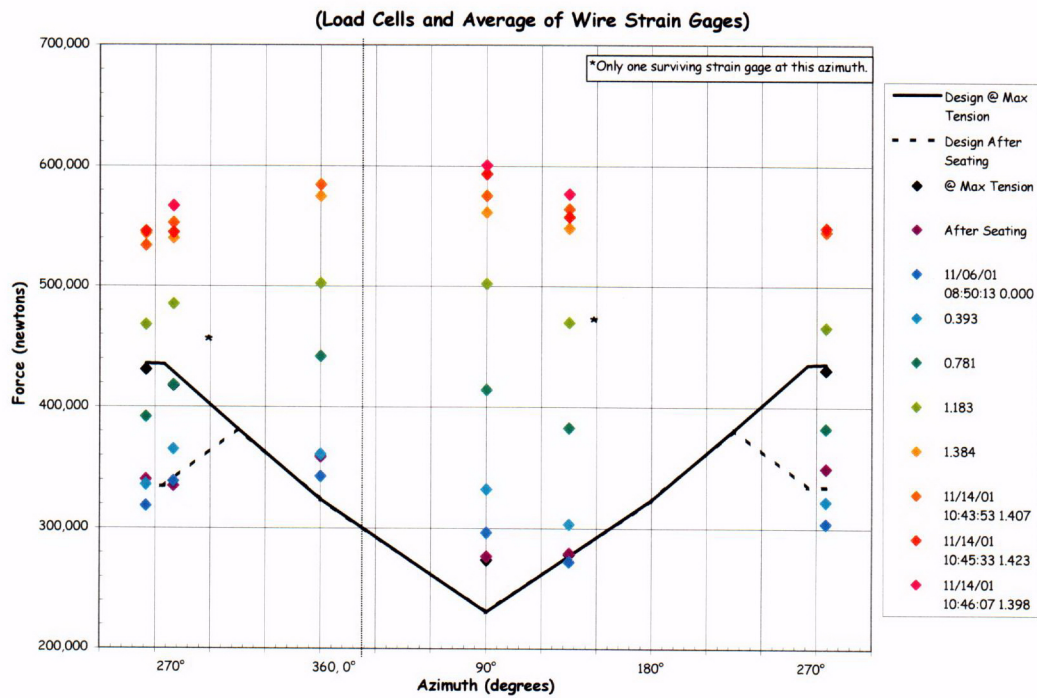


Figure 5.114 SFMT - Tendon H67 Force Distribution (Elev. 8153)

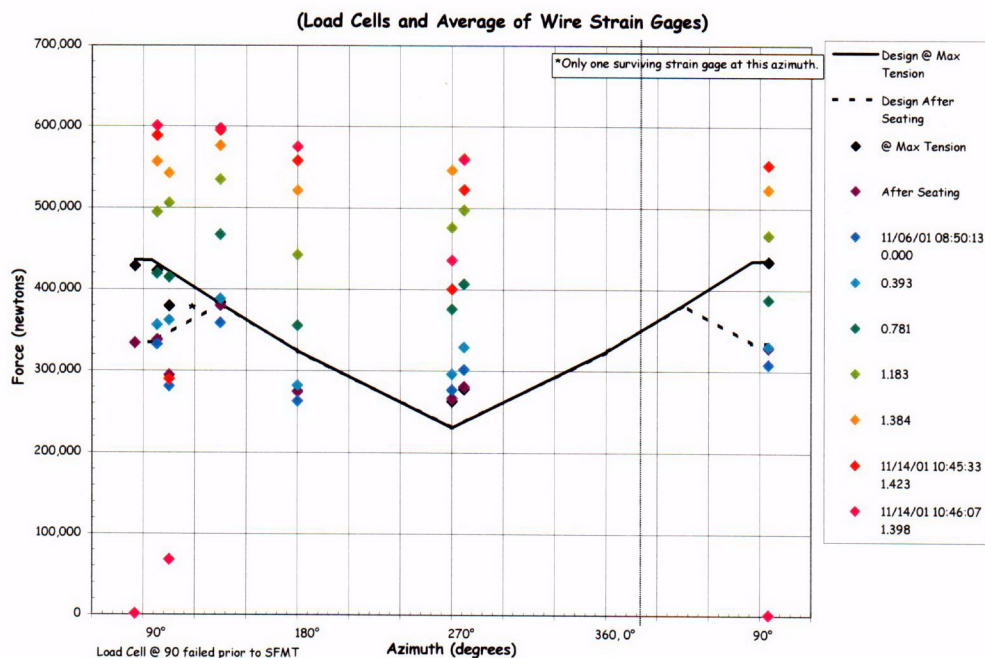


Figure 5.115 SFMT - Tendon H68 Force Distribution (Elev. 8280)

Again, the data is not adequate to assume the shape of the hoop tendon force profile between the surviving measurement positions, and only the force at the measurement locations are plotted, with no attempt to interpolate the strain between the measurement locations. As the pressure is increased, however, and generalized yielding of the model and the tendons occurs, all the plots indicate that the tendon force becomes more uniform along the length, approaching a limiting value of approximately 600 kN (135 kips). One unresolved issue is whether the tendon force equilibrates by slipping relative to the sheath or if the friction is high enough to effectively bond the tendon to the concrete.

An attempt was made to determine this by calculating the local, displacement-based strain in the wall and, assuming the tendon behaved as if bonded, adding it to the initial prestressing strains and computing the force profile from these strains. Figure 5.116 compares the force distribution obtained in this manner with the forces based on the tendon strain measurements for tendon H35 near elev. 4680 where the displacements were measured. The results compare favorably and seem to reinforce the idea that the tendons behave as if they were bonded after prestressing. While this is a compelling argument, it must also be admitted that these results are not entirely conclusive and further tests may be required to resolve this issue.

Figures 5.117 to 5.119 show the force profiles for the instrumented vertical tendons. Again, as was observed with the response during the LST, the force profile appears to become more uniform with pressure. Since the vertical tendons do not yield, tendons must slip relative to the sheath or concrete wall, even in the dome where the tendons are curved. This counters the observation made for the hoop tendons that the tendons behave as if they were bonded to the concrete. No explanation for this apparent inconsistency has been proposed, reiterating the need for further investigation of this behavior, including additional testing.

5.3.3.1.5 Acoustic Response

The acoustic monitoring system used during the LST was also employed for the SFMT, minus the interior sensors, which were removed to install elastomeric liner. Since the SFMT was not focused on detecting liner tearing/leaks, this was not a significant compromise. The focus of the acoustic system during the SFMT was to detect tendon wire breaks and any other events that might indicate structural damage. The acoustic monitoring system was put into operation at the same time the main DAS was started, prior to filling the vessel with water. (As noted in Section 5.2, it was also employed during the pneumatic leak check of the elastomeric liner.)

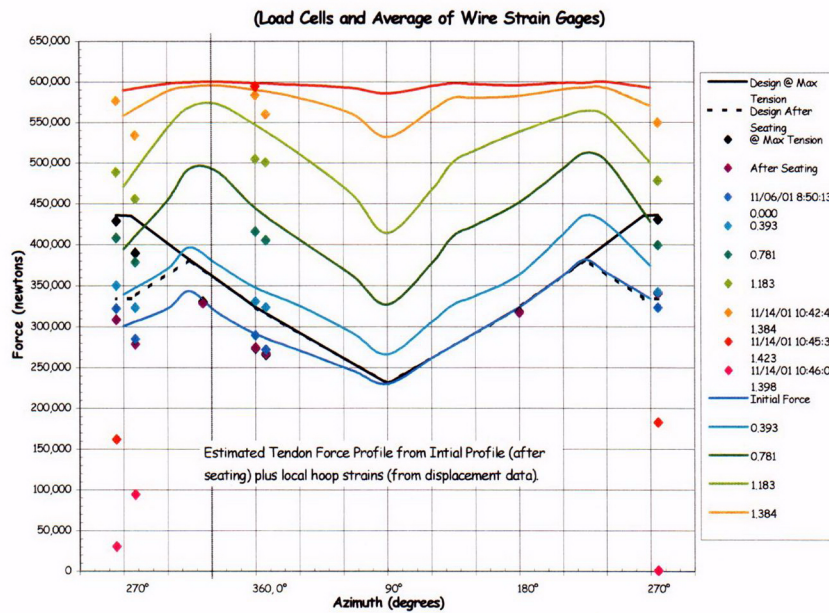


Figure 5.116 SFMT – Tendon H35 Computed and Measured Force Distribution

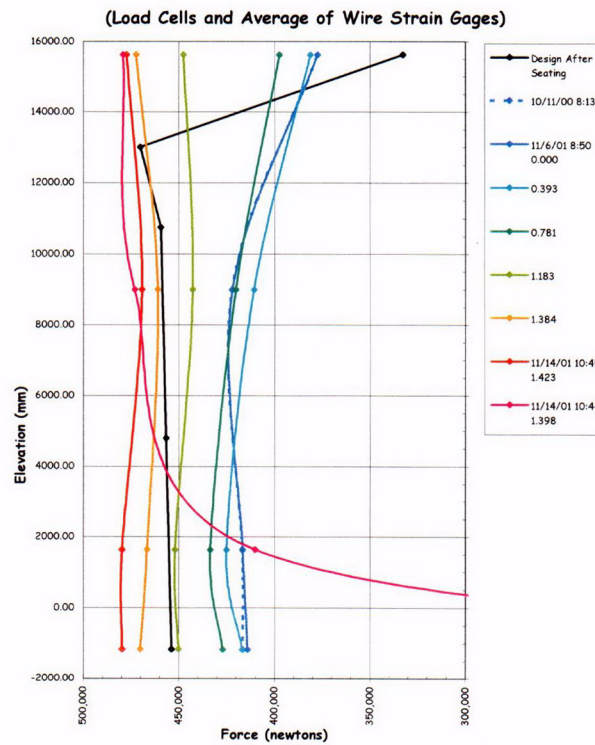


Figure 5.117 SFMT - Tendon V37 Force Distribution at Azimuth 240 Degrees

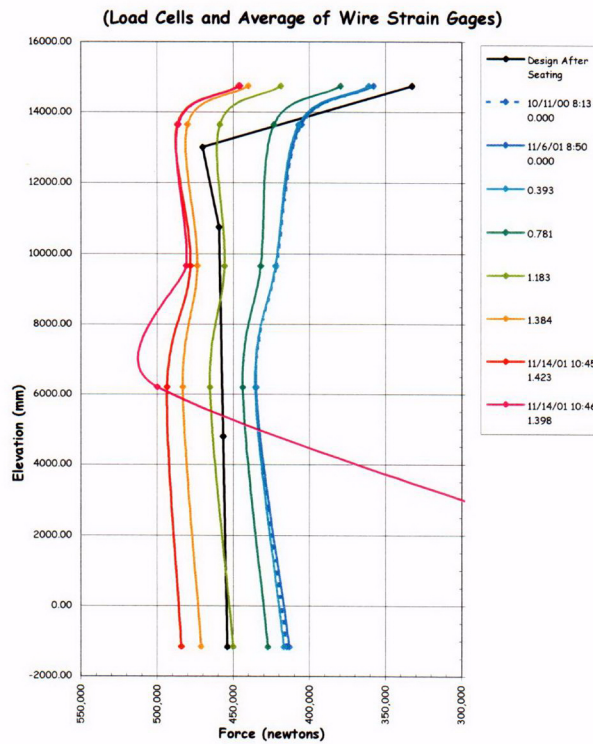


Figure 5.118 SFMT - Tendon V46 Force Distribution at Azimuth 135 Degrees

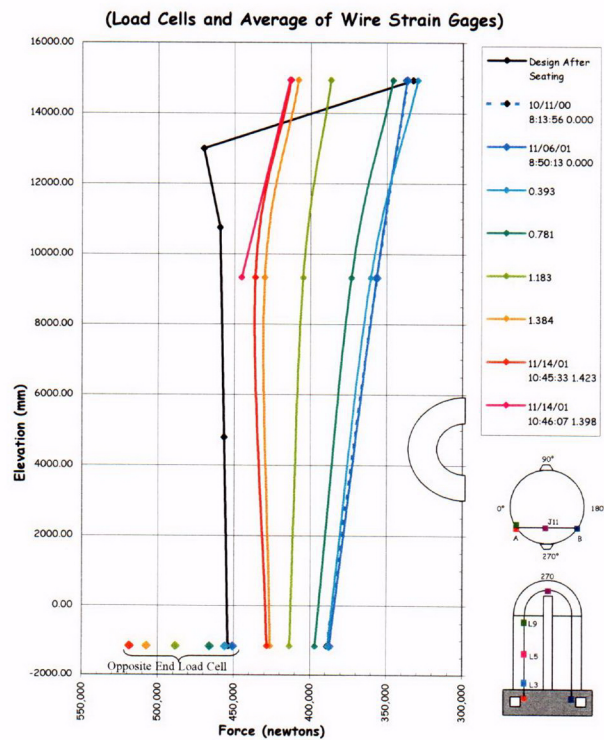


Figure 5.119 SFMT - Tendon V85 Force Distribution at Azimuth 325 Degrees

The post-SFMT reports from Pure Technologies are included in Appendix K. The acoustic event data is also included with the SFMT response data files in Appendix I (data CD). Along with a .wav file of the combined acoustic output during the final minute leading up to, and including, the rupture of the PCCV model. In addition to background noise associated with leaking, deformation, and microcracking of the model, the system identified distinct acoustic events which were categorized as concrete cracking, tendon gallery events, tendon pings, and tendon wire breaks.

Only 27 distinct concrete cracking events were recorded during the SFMT prior to rupture, continuing the trend observed during the LST, i.e., the bulk of the concrete cracking events occurred between 1.0 and 2.3 P_d . The tendon pings were confined to the vertical buttresses and the tendon gallery, as during the LST, suggesting the tendons and anchors continued to readjust or reseat themselves. Since all the tendon pings occurred during the final minutes of the SFMT (10:39:30 to 10:45:26), it may also suggest some slipping at the anchors.

The tendon gallery events were all limited to the tendon gallery between 10:43:37 and 10:46:03, implying something occurred with the vertical tendons. The acoustic characteristic of these events is different from the tendon pings and suggested a different mechanism. However, no physical explanation for these events was offered or identified during posttest inspection or demolition of the model.

Fifty-seven actual or probable wire break events were identified between 10:39:47 and rupture of the model at 10:46:12. The wire-break event locations are mapped in Figure 5.120.

Other than observing the discontinuities in the tendon load cell and strain time histories that might indicate a wire break, there were no other efforts to correlate the probable wire breaks identified by the acoustic system with the other test data. While it is arguable that the probable wire break events were actual wire breaks, at least a dozen or so were confirmed by the visual records. Figure 5.121 plots the time history of all the acoustic events along with the effective pressure time history. It is readily apparent that the frequency and magnitude of the wire break events increases just prior to rupture.

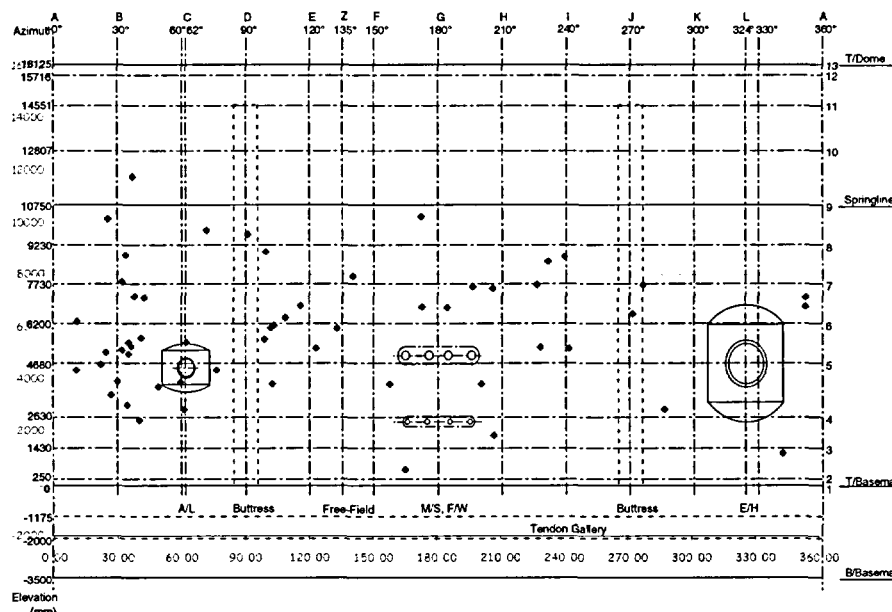


Figure 5.120 SFMT – Wire Break Map

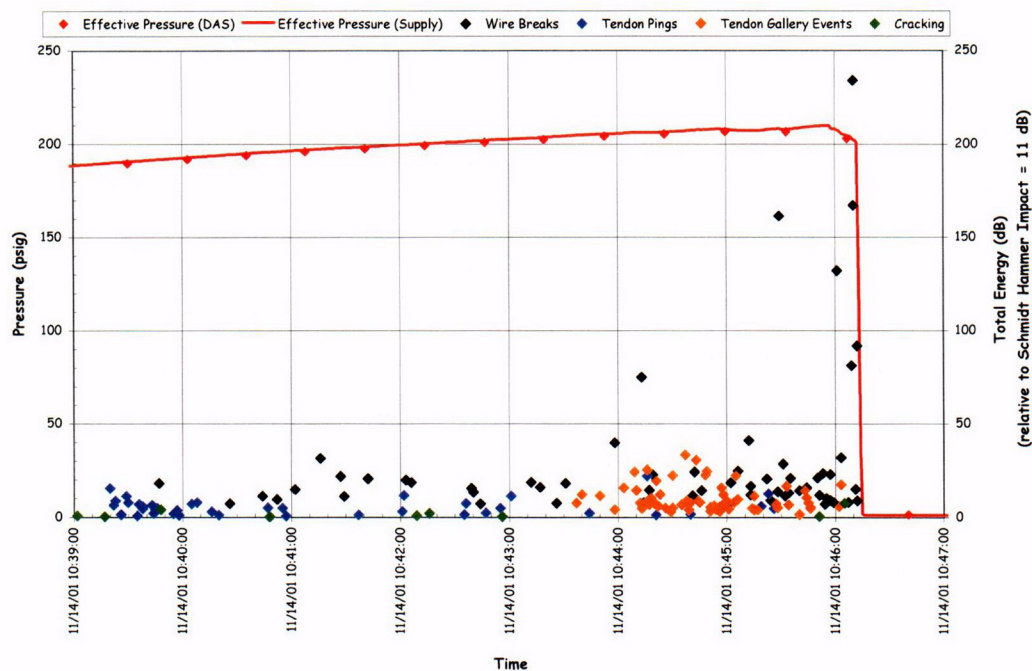


Figure 5.121 SFMT – Acoustic Event and Pressure Time History

5.3.3.1.6 Video

Due to the dynamic nature of the PCCV model rupture at the end of the SFMT, the video images were a valuable diagnostic resource for understanding the failure sequence. Four exterior digital video cameras at 0 degrees, 90 degrees, 180 degrees, and 270 degrees and two interior video cameras at the E/H and at the top of the dome monitored the model throughout the SFMT. Viewing the images in slow motion revealed that the model rupture began at the mid-height of the cylinder at approximately 6 degrees azimuth. The rupture propagated vertically in both directions until it reached a point approximately 2 m above the top of the basemat. The cylinder wall then began to open up, shearing itself from the basemat circumferentially in both directions, and meeting on the back side at 180 degrees. The vessel then ‘telescoped’ over the stem of the cylinder wall before coming to rest on the instrumentation frame.

The interior view of the E/H was distorted by the water and the resulting images were not useful. However, the camera in the dome showed the water surface dropping just prior to the rupture of the vessel, which was captured by all four external video cameras. A video file (.mpg) showing the PCCV model during the final minute of the SFMT and posttest images is included on the data CD in Appendix I. This video includes the acoustic system recording synchronized with the visual images. From close inspection of the video file, visible event times were documented in Table 5.6. The same event may have been observed at slightly different times depending on the camera viewing the event.

5.3.3.2 Posttest Inspection

Since the model was severely damaged and unstable, inspection after the SFMT was limited to an exterior survey. The exterior surface was photographed and the debris field was roughly mapped to document the model fragment locations.

The rupture lines are roughly mapped in Figure 5.122. This figure shows the approximate location of major vertical and horizontal rupture lines along with secondary tears at the E/H and adjacent to the main vertical rupture. These secondary tears are most likely associated with previous liner tears and/or cutouts.

The hoop rebar and tendons along the main rupture line were also inspected for evidence of any discontinuity or other defects that may have accounted for the location of rupture. The close-up photographs of the rebar and tendon strands in Figure 5.123 clearly show ‘necking’ of the bars and wires, indicating that they failed in a ductile manner with large local strains occurring before failure. These photographs are typical of all the tendons and bars at the rupture. The hoop

Table 5.6 SFMT Video Event Times

Time	0° Camera	90° Camera	180° Camera	270° Camera
hour:min:sec:1/30th sec (Video camera speed: 30 frames/second)				
10:45:55:28		H40 wedge ejected, strand broken		
10:45:56:01			H40 wedge ejected, strand broken(?)	
10:45:56:15		Something begins falling @ 100°, El. 5000 toward 5 o'clock		
10:45:56:26	Concrete spall above E/H			
10:45:57:00				Concrete spall (?) @ E/H
10:46:01:24		H42 wedges ejected, strand broken	H42 wedge ejected, strand broken	
10:46:03:10	Water stream starts @ 30°			
10:46:09:09		H64 strand broken/ejected		
10:46:09:12			H64 strand ejected	
10:46:11:21		Spurt of water(?) from H48 anchor		
10:46:11:26	H37 strand ejected			H37 strand ejected
10:46:12:00	Rupture initiated @ 6° (Collapse over in less than 2 seconds)			
10:46:12:01			H40 second strand ejected H37 strand ejected	Rupture
10:46:12:06			Rupture, multiple strands ejected	

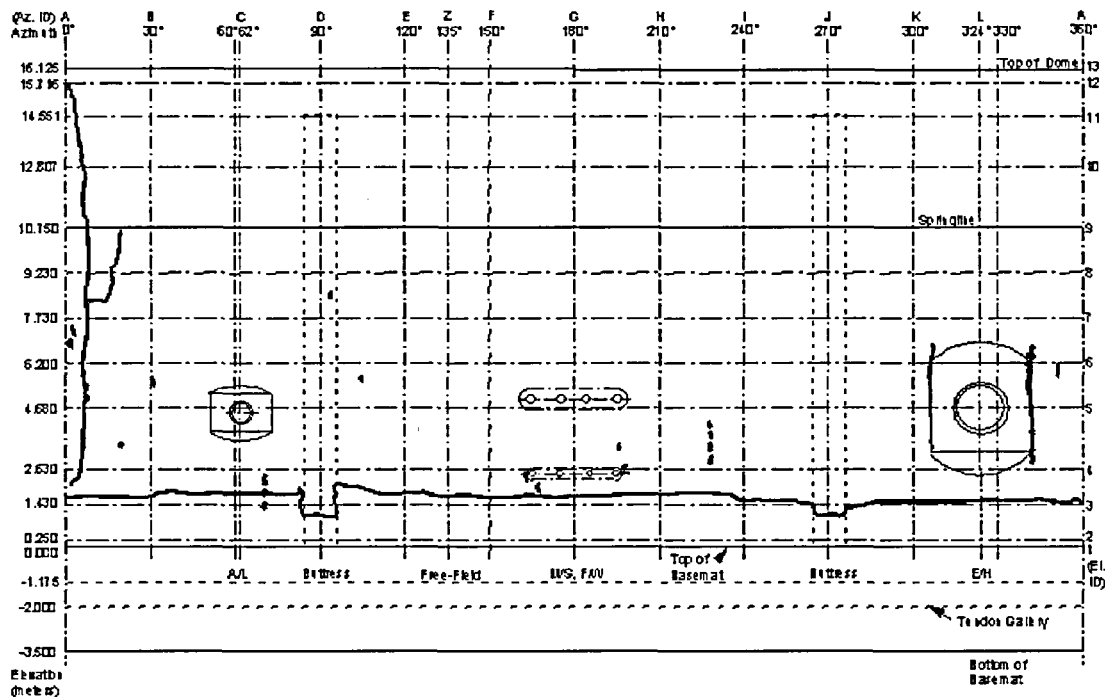


Figure 5.122 SFMT – Rupture Map

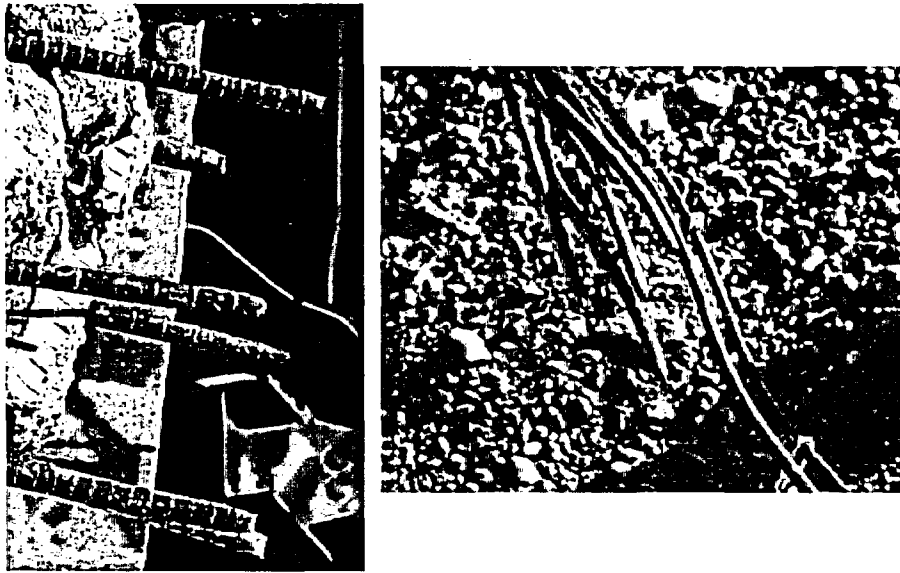


Figure 5.123 SFMT – Rebar and Tendon Strands at the Rupture Line

bars were spliced mechanically very near the rupture, but there was no evidence that any of the mechanical splices failed or that these in any way biased the location where failure began.

The position of the model after the SFMT was also noted. Figure 5.124 shows that the model displaced approximately 3" horizontally and tipped in the opposite direction of the rupture. Six tendons were completely ejected from the model and the final location of major pieces of debris were mapped on the site plan, as shown in Figure 5.125. The location of the debris was not only due to the initial rupture, but also by the flow of 350,000 gallons of water escaping from the model.

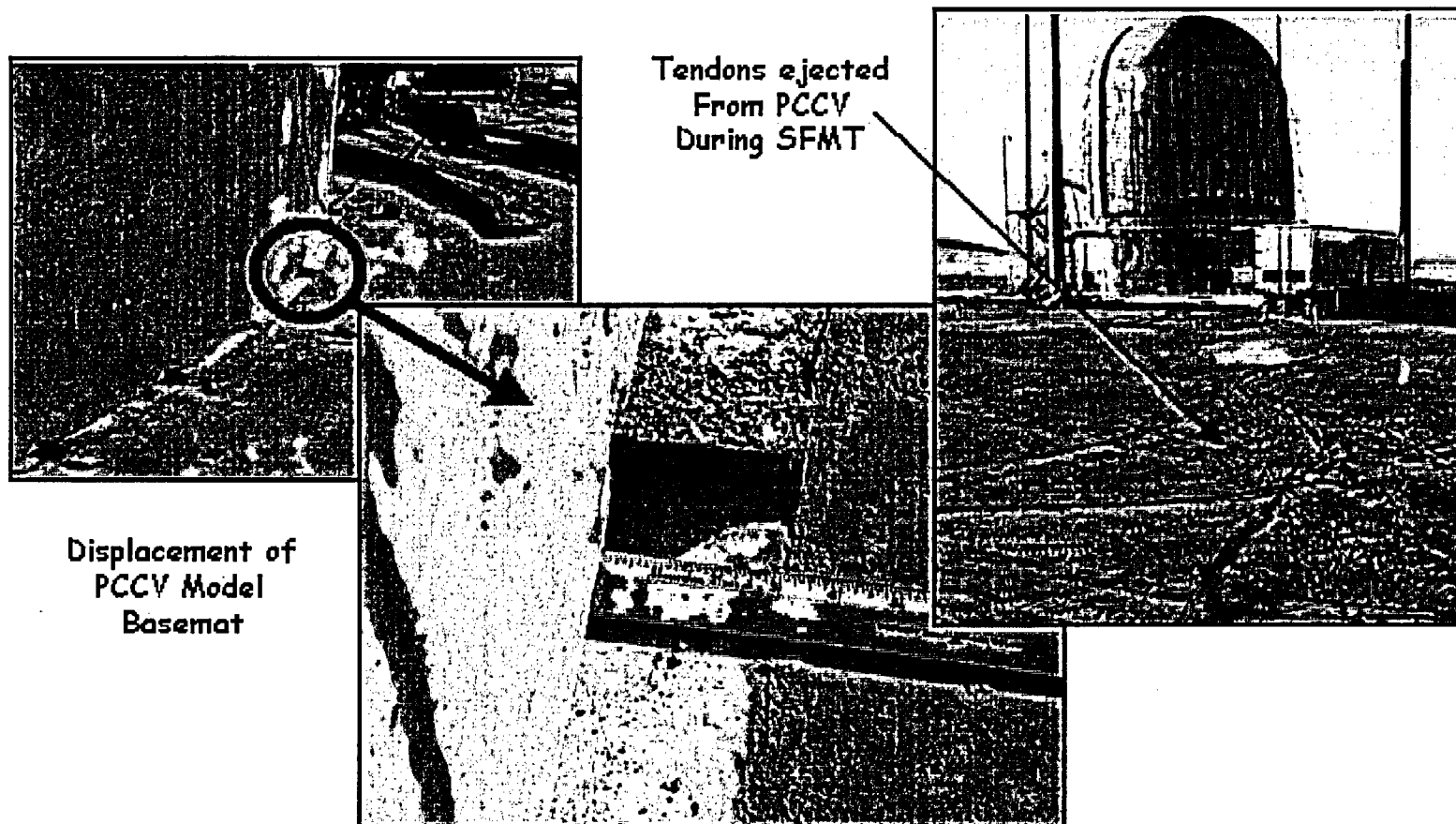


Figure 5.124 SFMT – Model Displacements

